Journal of
Materials Chemistry C

PAPER

View Article Online
View Journal | View Issue

Cite this: *J. Mater. Chem. C*, 2019, 7, 11152

Self-doping n-type polymer as a cathode interface layer enables efficient organic solar cells by increasing built-in electric field and boosting interface contact†

Yufei Wang, ‡[a] Zezhou Liang, ‡[a] Xiaoming Li,[b] Jicheng Qin,[a] Meiling Ren,[a] Chunyan Yang,[a] Xichang Bao, *[c] Yangjun Xia [a] and Jianfeng Li *[a]

Self-doped polymer cathode interface materials for organic solar cells have been widely investigated to enhance the ohmic contact between the electrode and the photoactive layer. Herein, a novel polymer named PBTA-FN with self-doping effect was successfully synthesized by incorporating benzotriazole (BTA) as an electron-deficient group and a fluorene containing an amino group. In favor of the n-type backbone and amine-based groups, an obvious n-type doping was obtained, resulting in the dramatically improved conductivity of PBTA-FN. Subsequently, PBTA-FN and PFN as cathode interface layers (CILs) were successfully applied in the organic solar cells based on PBDB-T-2F:IT-4F. A notable power conversion efficiency of 12.18% and 11.03% could be achieved with PBTA-FN and PFN as CILs, respectively. PBTA-FN showed better planarity than PFN as observed from the results obtained *via* density functional theory. The self-doping behaviour of PBTA-FN was determined by electron paramagnetic resonance, which exhibited a higher mobility and carrier density. The water contact angle results on the surface of the active-layer/PBTA-FN bilayer suggested that the PBTA-FN surface polarity was improved, which was attributed to the larger interface dipole. Thus, PBTA-FN can reduce the work function of an Al electrode and enhance the built-in electric potential, which were further confirmed by ultraviolet photoelectron spectroscopy and Mott Schottky curves, and the related device produced a higher V_{oc} (0.88 V) than PFN (0.86 V). This work provides a deeper understanding of the PBTA-FN interlayer mechanism and has a potential application in optoelectronic devices.

Received 29th June 2019,
Accepted 8th August 2019

DOI: 10.1039/c9tc03506k

rsc.li/materials-c

Introduction

Organic solar cells (OSCs) have great potential in curbing the energy issues, owing to the advantages such as low-cost, roll-to-roll fabrication, flexibility and light-weight.[1–10] In the past several decades, the power conversion efficiency (PCE) of OSCs has already exceeded 14% due to the efforts of numerous researchers.[11–18] Various strategies have been implemented to improve the performance of OSCs, such as designing new photoactive layer materials, new device structures, optimizing photoactive layer morphology and interface engineering.

Among various methods, interface engineering has been the simplest and most effective way for improving the performance of OSCs. A series of cathode interface materials (CIMs) were produced accordingly, mainly divided into inorganic CIMs and organic CIMs. Some traditional inorganic CIMs including ZnO, LiF, TiO_x and Al_2O_3, have already been successfully used in OSCs.[19–21] However, some disadvantages such as surface defects, high temperature annealing and poor contact with the active layer were also exposed. In contrast, alcohol-soluble conjugated organic CIMs with the virtue of low temperature processing, good ohmic contact and simplified device process have been widely studied. Commonly, alcohol-soluble conjugated polymers (ASCPs) were designed based on p-conjugated chain and polar side chain groups that can be dissolved in water or alcohols. For examples, poly[(9,9-bis(3′-(*N*,*N*-dimethylamino)-propyl)-2,7-fluorene)-*alt*-2,7-(9,9-dioctylfluorene)], named PFN, synthesized by Cao *et al.*, has been successfully used in OSCs to realize high PCE.[22] However, the conductivity of ASCPs is poor, which limits the improvement in PCE. The n-type self-doping for ASCPs is an effective means to achieve higher

[a] *School of Materials Science and Engineering, Lanzhou Jiaotong University, Lanzhou, 730070, P. R. China. E-mail: ljfpyc@163.com*
[b] *College of Chemistry and Pharmaceutical Engineering, Hebei University of Science and Technology, Shijiazhuang 050018, P. R. China*
[c] *Qingdao Institute of Bioenergy and Bioprocess Technology, Chinese Academy of Sciences, Qingdao 266101, P. R. China*

† Electronic supplementary information (ESI) available. See DOI: 10.1039/c9tc03506k

‡ Yufei Wang and Zezhou Liang contributed equally to this work.

electrical conductivity.[23,24] Some self-doping materials comprising p-deficient backbones, such as perylene diimide, and fullerene, were designed and synthesized as a promising way for designing new CIMs.[25,26] However, few reports could be found on using the benzotriazole p-deficient group for preparing CIMs.

In this study, an alcohol-soluble conjugated polymer named PBTA-FN based on fluorene and benzotriazole derivatives was designed and synthesized. PBTA-FN is eco-friendly, can be prepared in the room temperature without further annealing and can dissolve in methanol under the presence of a small volume of acetic acid (3% vol to methanol),. The chemical and physical properties of PBTA-FN were systematically investigated, and the fascinating self-doping behavior was determined by electron paramagnetic resonance (EPR). PBTA-FN could form a better ohmic contact at the interface and possessed higher electron mobility than PFN. The photovoltaic performance based on PBTA-FN and PFN as CIMs and PBDB-T-2F:IT-4F as active-layer was investigated: open circuit potential (V_{oc}) increased from 0.86 V to 0.88 V, short current density (J_{sc}) increased from 18.15 to 19.06 mA cm^{-2}, and fill factor (FF) raised from 70.54% to 72.65%.

Experimental section

Materials and reagents

PBDB-T-2F and IT-4F were obtained from Organtec solar materials Inc. Chlorobenzene and phenyl sulfide were acquired from Sigma-Aldrich and J&K Chemical Ltd, respectively. The synthesis route of PBTA-FN is shown in the ESI.†

Device fabrication and characterization

The conventional photovoltaic device was prepared with ITO/PEDOT:PSS/PBDB-T-2F:IT-4F/CIL/Al structure (Fig. 2a). The indium tin oxide glass (ITO) used for the substrate was first subjected to ultrasonic cleaning by deionized water, acetone, deionized water and isopropanol, in sequence. Then, a PEDOT:PSS thin film (40 nm) was spin coated on the ozone-treated ITO substrate. The photoactive layer PBDB-T-2F:IT-4F, after addition of 0.5% DPS (diphenyl sulfide) (total concentrations 20 mg mL^{-1}, 1 : 1), was dissolved in chlorobenzene. After a 100 nm photoactive layer film was formed on the PEDOT:PSS thin film through the spin-coating method, the photoactive layer was annealed at 100 1C under hot table. Next, various CILs (w/o, PFN, PBTA-FN) were formed using the same procedure. Finally, a 100 nm Al electrode was deposited by thermal evaporation.

The test conditions for AFM, ^{1}HNMR, UV-visible spectroscopy, CV (cyclic voltammetry), *J*–*V* (current density-curve), and EQE (external quantum efficiency) were as same as those used in our previous paper,[27,28] while the measurement environment for impedance spectroscopy and the capacitance–potential curve were identical to ref. 29. The ultraviolet photoelectron spectroscopy (UPS) curves of the photovoltaic devices were recorded on AXIS ULTRA DLD (Kratos, Japan). Electron paramagnetic resonance spectroscopy curves were recorded using A300-9.5/12 (Bruker, Germany).

Results and discussion

Optical and electrochemical performance of PBTA-FN

A UV-visible spectrometer (UV-1800) and an electrochemical workstation (CHI660D) were used to characterize the optical and electrical properties of PBTA-FN, respectively. The UV-visible spectrum and the calculated results of PBTA-FN film (film 1) are exhibited in Fig. 1a and Table 1, respectively. The maximal absorption peak ($\mathbf{l}_{absmax}$) is located at 424 nm. The optical band gap (E_g) was 2.53 eV, obtained from 490 nm by using the required formula (eqn (S1), ESI†). In order to study the effect of the introduction of PBTA-FN on the light absorption properties of a photoactive layer, the normalized absorption spectra of PBDB-T-2F:IT-4F (film 2), PBDB-T-2F:IT-4F/PFN (film 3), and PBDB-T-2F:IT-4F/PBTA-FN (film 4) were recorded. As shown in Fig. 1a, the absorption spectra of film 1 and film 2 are almost coinciding, which indicates that the introduction of PFN did not contribute to the absorption of the OSCs. However, the absorption of the OSCs with PBTA-FN improved in the range from 332 nm to 540 nm, which could lead to a higher J_{sc} than that of PFN.

The electrochemical curve of the PBTA-FN film is shown in Fig. S1 (ESI†), and the onset redox potential (E_{ox}) was determined to be 0.71 V when the reference electrode used was $Ag/AgNO_3$. On the basis of the eqn (S1)–(S3) (ESI†), the energy level of the highest occupied molecular orbital (E_{HOMO}) and the corresponding lowest unoccupied molecular orbital (E_{LUMO}) of PBTA-FN were —5.35 and —2.76 eV, respectively, which are listed in Table 1.

Electron paramagnetic resonances

Electron paramagnetic resonance (EPR) spectroscopy is used to study the self-doping behavior of polymers, because it can determine the formation of free radicals.[30] For comparison, PFN and PBTA-FN as mass solids of uniform quality were used for EPR tests under light (405 nm) trigger, and the related results are shown in Fig. 1b. PBTA-FN exhibited a positive paramagnetic response and a g-value of 2.005 (Fig. S2, ESI†),[31] while PFN basically had no signal response, indicating that the free radicals are formed in solid state PBTA-FN. The amine group was able to provide electrons to the conjugated electron-deficient group, resulting in a substantial doping behavior.[30] Thus, the appeared EPR signal was attributed to the amine group of PBTA-FN donating electrons to the BTA electron-deficient group, thus establishing the self-doping behavior of

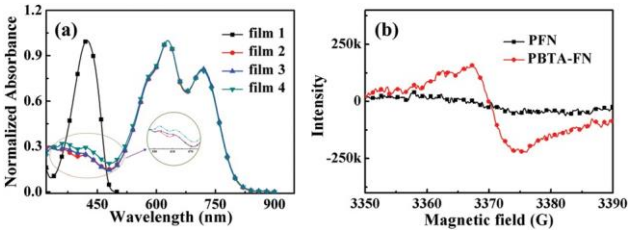

Fig. 1 (a) Normalized absorption of the PBTA-FN film and PBDB-T-2F:IT-4F blend film using different CILs; (b) EPR spectra of PFN and PBTA-FN under solid state.

Table 1 The parameters of optical and electrochemical properties for the PBTA-FN film

Polymer	λ_{absmax} (nm)	λ_{edge} (nm)	E_g^{opt} [a] (eV)	E_{ox} (V)	E_{HOMO} [b] (eV)	E_{LUMO} [b] (eV)
PBTA-FN	424	478	2.59	0.71	—5.35 (—5.04[c])	—2.76 (—1.92[c])

[a] E_g^{opt} was calculated from eqn S1 (ESI). [b] The values of E_{HOMO} and E_{LUMO} were obtained from eqn (S2) and (S3) (ESI). [c] The corresponding values were determined by density functional theory (DFT) at the B3LYP-D3(BJ)/6-31G level (ESI).

PBTA-FN. The strong self-doping behavior of PBTA-FN could improve the charge transport ability and carrier density, which results in a higher electron mobility, indicating that effective doping can improve the carrier density in the doped films.[32] The lack of an EPR signal in PFN was ascribed to the weak conjugated electron-deficient group and high LUMO level of the polymer backbone.[31]

Theoretical calculations

The geometry of PBTA-FN was optimized at the B3LYP-D3(BJ)/6-31G level by density functional theory (DFT) calculations.[33] The side chains were ignored and replaced by hydrogen atoms to simplify the calculations. The result indicated that PBTA-FN has better linear configuration than PFN, as shown in ESI.† PBTA-FN exhibits a LUMO level of —1.92 eV and a HOMO level of —5.04 eV.

Photovoltaic performance of PBTA-FN

In order to reflect the role of PBTA-FN in the photovoltaic performance in a better way, we chose OSCs without interface and PFN (0.2 mg mL^{-1}) as references. The *J*–*V* curves and the correlative EQE curves are displayed Fig. 2c and d, respectively. The photovoltaic parameters of OSCs are listed in Table 1. As shown Fig. 2c, PBDB-T-2F:IT-4F without CILs delivered a low V_{oc} (0.44 V) and poor FF (42.82%), resulting in a PCE of 3.21%.

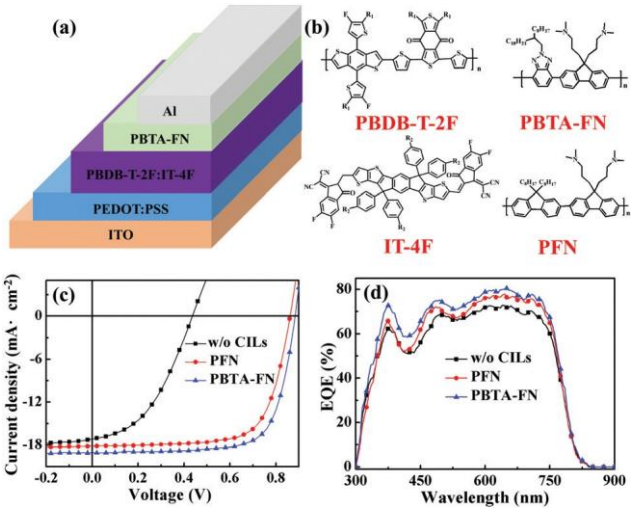

Fig. 2 (a) Architecture of the OSCs and (b) the molecular structure obtained in this study; (c) *J*–*V* curves and (d) EQE spectra of a photovoltaic device based on PBDB-T-2F:IT-4F under different conditions.

After inserting PFN (0.2 mg mL^{-1}) as the CIL, the photovoltaic performance was improved significantly, and the PCE reached 11.03%. Furthermore, the highest PCE of 12.18% could be obtained when PBTA-FN was inserted in between Al and the PBDB-T-2F:IT-4F layer. The improved device performance is attributed to higher V_{oc} (0.88 V), J_{sc} (19.05 mA cm^{-2}) and FF (72.65%). The J_{sc} values obtained from *J*–*V* curves were confirmed by EQE curves (Fig. 2d), and the deviation in J_{sc} values acquired from the *J*–*V* curves and EQE spectra are within 5%. As displayed in Fig. 2d, the addition of CILs doesn't change the shape of the EQE curves, and the EQE value reached maximum when using PBTA-FN as the CIL. Furthermore, the R_s (series resistance) and R_{sh} (parallel resistance) values were calculated. As shown in Table 2, R_s distinctly decreased while R_{sh} increased with the addition of CILs, respectively. The best R_s (4.44 Ω cm^2) and R_{sh} (4758.51 Ω cm^2) values were obtained with the introduction of PBTA-FN, indicating that PBTA-FN can promote charge extraction and reduce the charge accumulation at the interface; thus, the charge collecting ability becomes stronger, which is consistent with higher FF and J_{sc}.

To illustrate the effect of PBTA-FN on charge generation and recombination, the J_{ph} *versus* V_{eff} curves of photovoltaic devices with different treatment conditions are characterized in Fig. 3a. Herein, J_{ph} obeys the $J_{ph} = J_L - J_D$ relation, where J_L and J_D refer to the current density under illumination and the current density under dark conditions, respectively. V_{eff} is the effective voltage, obeying the relationship $V_{eff} = V_0 - V_{appl}$, where V_0 refers to the voltage when J_{ph} is 0 and V_{appl} is the voltage applied across the photovoltaic device.[34] Clearly, the J_{ph}–V_{eff} curves were divided into two regions that indicated linear growth and saturation. The linear growth region emerged in V_{eff} ≤ 0.2 V when J_{ph} grew linearly with V_{eff}.

Then, J_{ph} slowly tended to a saturation value (J_{sat}) in the region of V_{eff} ≥ 1V. Therefore, the exciton dissociation rate $P(E,T) = J_{ph}/J_{sat}$ could be determined while maximum exciton generation rate was obtained from $G_{max} = J_{sat}/eL$, where *e* is the elementary charge and *L* is the photoactive layer.[35] The $P(E,T)$ against V_{eff} curves are exhibited in Fig. 3b and the correlative results are summarized in Table 1. At V_{eff} = 2.5 V, the J_{sat} values of OSCs were 18.55 mA cm^{-2} (w/o CILs), 18.73 mA cm^{-2} (PFN), and 19.57 mA cm^{-2} (PBTA-FN), and the corresponding calculated $P(E,T)$ values were 92.52%, 96.89%, 97.32%. Moreover, the highest G_{max} value of 1.11 × 10^{28} m^{-3} s^{-1} was obtained with PBTA-FN as a CIL, which was attributed to the stronger absorption of OSCs. Above all, PBTA-FN as the CIL of OSCs can obtain better exciton dissociation rate and production rate than PFN, which will further reduce the recombination loss, and thus help achieve the best J_{sc} and FF values.

To further explain the effect of self-doping behaviour of PBTA-FN on conductivity, devices with the ITO/CILs/Al structure were fabricated and tested by *I*–*V* mode under dark condition. The CIL thicknesses were controlled to 100 nm. The direct current conductivity (σ_0) is represented by the formula $I = \sigma_0 A d^{-1} V$, where *I* represents current, *A* is the area of the measured electrode (0.1 cm^2), *d* stands for the CIL thickness (100 nm), and *V* is the applied voltage.[36] As shown in Fig. 3c, when PFN was inserted

Table 2 Photovoltaic parameters of OSCs with different CILs

CILs	V_{oc} (V)	J_{sc} (mA cm^{-2})	FF (%)	PCE[a] (%)	R_s (Ω cm^2)	R_{sh} (Ω cm^2)	J_{sc}/J_{sat}	G_{max} (m^{-3} s^{-1})
w/o CILs	0.44 ± 0.05	17.16 ± 0.12(17.14)[b]	42.82 ± 0.14	3.21 ± 0.17	11.46	174.07	92.52%	1.05×10^{28}
PFN (5 nm)	0.86 ± 0.01	18.15 ± 0.11(18.10)	70.54 ± 0.21	11.03 ± 0.23	5.29	2107.04	96.89%	1.06×10^{28}
PBTA-FN (6 nm)	0.88 ± 0.01	19.05 ± 0.07(19.04)	72.65 ± 0.11	12.18 ± 0.19	4.44	4758.51	97.32%	1.11×10^{28}

[a] The PCE values were obtained from 15 cells. [b] The integrated J_{sc} values from EQE spectrums.

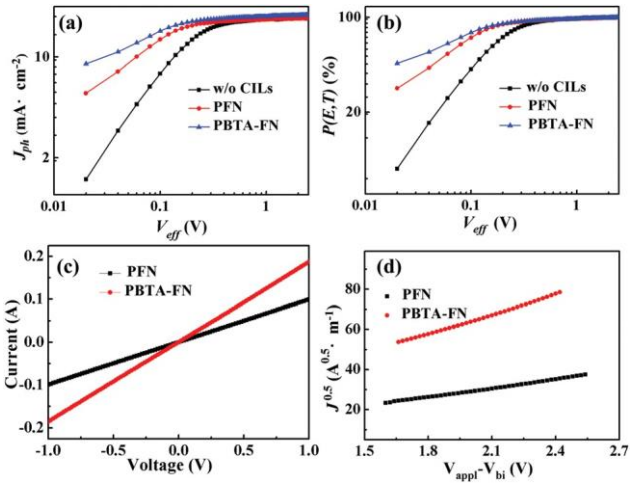

Fig. 3 (a) J_{ph} *vs.* V_{eff} curves and (b) $P(E,T)$ *vs.* V_{eff} plots of OSCs with various processed CILs; (c) *I–V* curves of OSCs with ITO/CILs/Al structure; (d) fitting curves of electron-only devices with SCLC formula (eqn (S4),ESI†).

between ITO and Al electrode, a low value of the slope was obtained, corresponding to a poor conductivity value. However, when PBTA-FN was used as the interface, the slope enhanced significantly and good conductivity was obtained. This result indicates that the self-doping behaviour can effectively improve the interface conductivity and enable the formation of a good ohmic contact.[37]

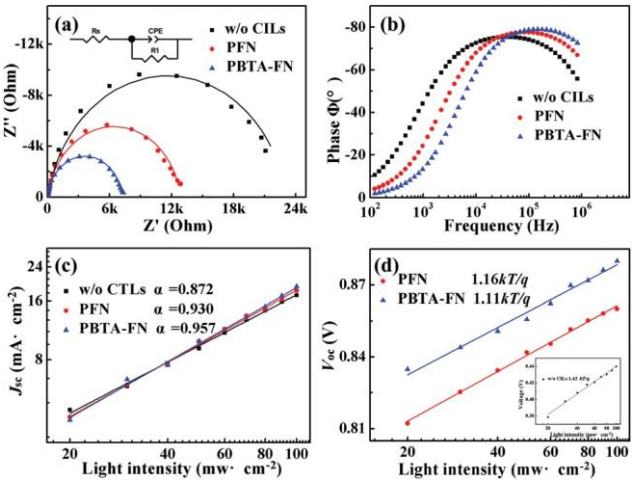

Fig. 4 (a) Nyquist plots and the equivalent circuit model (inset); (b) phase angle *vs.* frequency curves of OSCs with different CILs; (c) J_{sc} *vs.* P_{light} and (d) V_{oc} *vs.* P_{light} curves under different light intensity.

To comprehend the effect of PBTA-FN on photovoltaic performance, the electron-only devices with ITO/ZnO/PBDB-T-2F:IT-4F/CILs/Al configuration were prepared and measured according to the space charge limited current (SCLC) method, as shown in Fig. 3d. The electron mobility (m_e) of PFN was 1.06×10^{-4} cm^2 V^{-1} s^{-1}, while a m_e of 3.53×10^{-4} cm^2 V^{-1} s^{-1} was obtained for PBTA-FN as the CIL. The calculated result of electron mobility verified the fact that PBTA-FN with self-doping behaviour has higher electron mobility, so that high J_{sc} and FF can be obtained.

Carrier transport dynamics plays a crucial role in understanding device performance, so impedance spectroscopy (IS) for OSCs with different CILs processed was performed. The IS was performed in dark conditions with an open circuit voltage of 5 mV amplitude, with frequency ranging from 100 Hz to 1 MHz. The impedance spectra are composed of Nyquist curves and phase angle *vs.* frequency characteristics, where the phase angle and impedance Z determine the size of the resistance Z' and reactance Z''. The Nyquist plots of these devices are displayed in Fig. 4a; the symbol denotes as initial data and the solid line stands for fitting data by using an equivalent circuit (inserted into Fig. 4a). Moreover, the related resistance *vs.* frequency and reactance *vs.* frequency plots of OSCs with different CILs are displayed in Fig. S6 (ESI†). The equivalent circuit diagram for fitting the original data consists of a CPE and a resistor R_1 connected in parallel and then connected in series with a resistor R_s. According to Table 3, the fitted data shows a high quality match with the initial data and the error rate was less than 11%. In the equivalent circuit, R_s stand for a series resistor loss including ITO, photoactive layer, PEDOT:PSS and CILs, which was related to the intersection of the semi-circle with Z' axis at high frequencies, R_1 was related to charge recombination process.[38] In addition, CPE was a non-ideal capacitor with an inhomogeneous interface consisted of CPE-T and CPE-P. CPE-T represented the capacitor values and CPE-P was an ideal capacitor factor. It should be noted that CPE is a capacitor when CPE-P equal 1, while CPE is a capacitor with defects when CPE-P less than 1. Remarkably, R_s decreased from 24.17 Ω to 15.93 Ω with addition the of PFN, and R_s reached to

Table 3 Parameters of fitted data by using the equivalent circuit

CILs	R_s[a] (Ω)	R_1[a] (Ω)	CPE1-T (F)[a]	CPE1-P[a]	Error (%)
w/o CILs	24.17	23 155	2.50×10^{-8}	0.88	0.62–10.50%
PFN	15.93	12854	1.40×10^{-8}	0.91	0.42–10.47%
PBTA-FN	10.91	7210	1.04×10^{-8}	0.93	0.23–7.31%

[a] The fitting parameter values were obtained from the fitting software Zview.

the smallest value of 10.91 Ω on using PBTA-FN as the CIL, indicating that the introduction of CILs could enable the formation of a good ohmic contact between the photoactive layer and Al electrode.

Furthermore, the charge recombination resistor R_1 achieved the lowest value of 7210 Ω for OSCs with PBTA-FN, which indicates that PBTA-FN could suppress charge recombination effectively, thus improving FF and J_{sc}. Moreover, the CPE-P values of these OSCs were 0.88 (w/o CILs), 0.91 (PFN), and 0.93 (PBTA-FN). This indicates that a more uniform interface could be obtained by introducing PBTA-FN as the CIL, which was consistent with the results of AFM roughness.

The relationship between phase angle and frequency is exhibited in Fig. 4b, and the characteristic frequency (f_{max}) is defined by the frequency corresponding to the maximum phase angle point. The related charge transport time constant (t_{avg}) was determined through an expression:[39]

$$f_{max} \propto 1/t_{avg} \quad (1)$$

As shown in Fig. 4b, the f_{max} values of OSCs were 38 300 Hz (w/o CILs), 82 500 Hz (PFN), 147 000 Hz (PBTA-FN). The frequency peak result from Fig. 4(b) was further supported by Fig. S6 (ESI†). Therefore, when PBTA-FN was introduced in the OSCs, a small value of t_{avg} could be obtained, indicating that the carriers could reach the electrode in a shorter time, thereby obtaining higher J_{sc} and FF.[40]

We wished to further understand that the charge recombination of photovoltaic devices plays an important role in the performance of the device. Therefore, the OSCs with various processed CILs were measured under different light intensity. Fig. 4c and d show the plots of J_{sc} *vs.* P_{light} and V_{oc} *vs.* P_{light}, respectively. Generally, J_{sc} and P_{light} satisfy the relationship:

$$J_{sc} \propto P_{light}^{a} \quad (2)$$

where a denotes an exponential factor and P_{light} is referred to as light radiation intensity.[41] For photovoltaic devices without CILs, a minimum a value of 0.872 was obtained, corresponding to a severe bimolecular recombination. When PFN was used as the CIL, a value increased significantly to 0.930, indicating that the introduction of the PFN interface can suppress bimolecular recombination.[42] Remarkably, an a value of 0.957 (closest to 1) was obtained for OSCs with PBTA-FN as the CIL, resulting in higher FF and J_{sc} values. The result was supported by V_{oc} *vs.* P_{light} analysis. In Fig. 4d, the V_{oc} *vs.* P_{light} relations of OSCs under different conditions are displayed. Specially, the V_{oc} and logarithm of P_{light} obeys a linear relationship:

$$V_{oc} \propto \frac{nkT}{q} \ln(P_{light}) \quad (3)$$

where k and q are Boltzmann constant and elemental charge, respectively, and T and n are Kelvin temperature and slope, respectively.[43] The n value represents the dominant mechanism of the recombination process. When the value of n approaches 2, the main process is trap-assisted recombination, while the main process becomes bimolecular recombination when the value of n is 1.[44,45] In this study, the values of n were 1.42 (w/o CILs), 1.16 (PFN), and 1.11 (PBTA-FN). In the photovoltaic devices without CILs, two recombination mechanisms existed simultaneously and were comparable. Compared to PFN-treated OSCs, the bimolecular recombination process was the primary loss, and the trap-assisted recombination was suppressed. For photovoltaic devices using PBTA-FN, a minimum value of n was obtained, indicating that the bimolecular recombination was further reduced and the trap-assisted recombination was greatly inhibited.

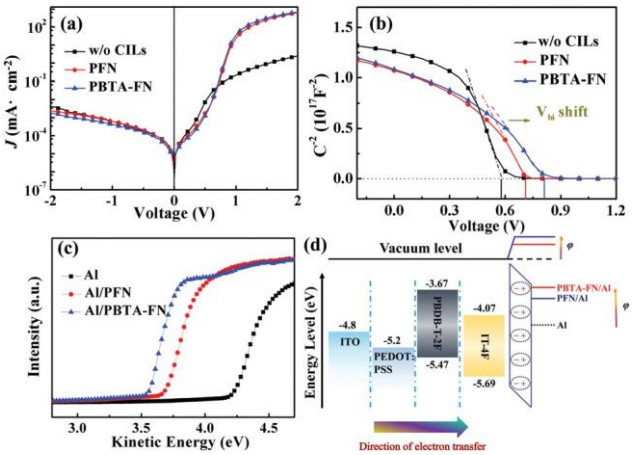

Fig. 5 (a) Dark current curves and (b) Mott Schottky curves of OSCs with different processed CILs; (c) UPS of Al electrode processed under different conditions; (d) energy level diagram.

To discern the reason for the improved photovoltaic performance, dark *J–V* curves of OSCs were recorded, as displayed in Fig. 5a. As shown in Fig. 5a, the reverse current density decreased on adding CILs (PFN or PBTA-FN) between the photoactive layer and Al, which indicated that the introduction of CILs could depress leakage current, thus resulting in a higher V_{oc}.[46] In the applied voltage region from 0 V to 2 V, the turn-on voltages were 0.38 V (w/o CILs), 0.67 V (PFN), 0.75 V (PBTA-FN). The high turn-on voltage reflected a higher built-in voltage, which could speed up the charge extraction and decrease the charge collection at the interface. The OSCs with PBTA-FN manifested a minimal leakage current and a higher turn-on voltage, promoting the implementation of high current and voltage, which was consistent with the small R_s and large R_{sh}.[47,48]

To study the effect of PBTA-FN on the work function (WF) of the Al electrode, the devices with the ITO/Al/CIL structure were fabricated and characterized by ultraviolet photoelectron spectroscopy (UPS). As shown in Fig. 5c, the WF of the bare Al electrode was exhibited to be 4.23 eV, while the work function of Al was pulled down to 3.69 eV after PFN processing. This reduced work function of 0.54 eV was attributed to the larger interface dipole; thus, a strong built-in field could be detected interface dipole; thus, a strong built-in field could be detected in the OSCs having PFN as the CIL. Specifically, the WF of Al decreased to 3.55 eV after PBTA-FN deposition and enabled in the formation of a larger interface dipole (Fig. 5d). The lowest WF (3.55 eV) could enable the formation of a better ohmic contact with the photoactive layer and increase the built-in field, which was beneficial to the enhanced charge extraction efficiency and the decreased recombination losses.[49]

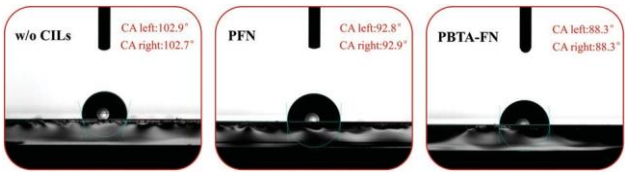

Fig. 6 Water contact angle of PBDB-T-2F:IT-4F blend film surface with different processed CILs, the insets "CA left" and "CA right" stand for an angle value calculated by left side and right side, respectively.

The wettability of CILs on a photoactive layer (PBDB-T-2F:IT-4F) was determined by water contact angle (WCA) measurements in order to understand the surface polarity.[50] The water contact angles (y) of the PBDB-T-2F:IT-4F blend film with different processed interfaces are displayed in Fig. 6, and the average y values were 102.81 (w/o CILs), 92.81 (PFN), and 88.31 (PBTA-FN). After the deposition of CILs, the WCA distinctly decreased, and the reduced y value indicated that the polar groups accumulated on the PBDB-T-2F:IT-4F blend film.[50] Specifically, the PBDB-T-2F:IT-4F film with the deposition of PBTA-FN obtained the smallest y (88.31), which clearly indicates the greater accumulation of the polar components; thus, better hydrophily could be seen.[51] Although the Al electrode was not deposited on the CILs and the interface contact had not been determined, the better hydrophily could improve contact.[52] Based on the UPS test results, inserting PBTA-FN between the active layer and the Al electrode could produce a larger interface dipole than PFN, which was attributed to the smaller water contact angle of PBTA-FN.[53] Thus, a better charge extraction and collection ability could be realized in the OSCs.

The effect of PBTA-FN on the morphology of the PBDB-T-2F:IT-4F blend film surface was further studied by AFM tests under tapping mode. As shown in Fig. 7a–c, the root-mean-square (RMS) values of the PBDB-T-2F:IT-4F film without CILs and with PFN or PBTA-FN were 2.39 nm, 2.41 nm, 2.13 nm, respectively. These results indicated that there was no obvious alteration in surface roughness for the PBDB-T-2F:IT-4F film using PFN or PBTA-FN. The similar 3D height images (Fig. 7d–f) further verified this argument, which resulted from the CILs (PFN and PBTA-FN) being very thin and not dissolving the photoactive layer. Thus, there was no need to worry about the corrosion of PBTA-FN on the PBDB-T-2F:IT-4F film. Moreover, the slightly smooth surface of PBDB-T-2F:IT-4F with PBTA-FN could improve the performance of the device in other aspects (impedance spectroscopy results).

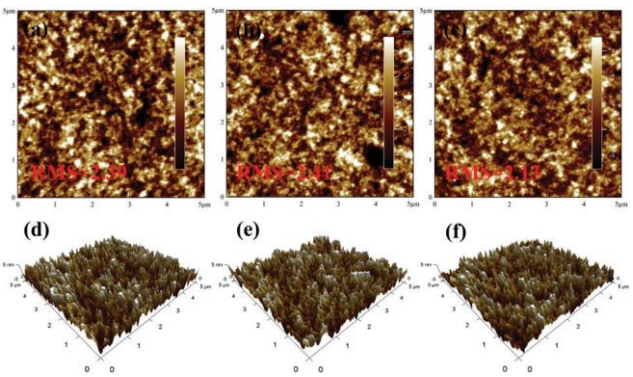

Fig. 7 AFM height images of PBDB-T-2F:IT-4F films with different CILs: (a) w/o CILs, (b) PFN, and (c) PBTA-FN; corresponding 3D height images (d–f).

In order to quantitatively explain the impact of PBTA-FN on the built-in electric field, the capacitance–voltage (C–V) measurements of OSCs with different CILs were carried out. The test condition of C–V was at a frequency of 1 kHz in a dark environment. The related Mott Schottky (C^{-2}–V) curves of these photovoltaic devices are depicted in Fig. 5b, and the built-in potential (V_{bi}) could be determined by the equation[54]

$$\frac{1}{C^2} = \frac{2(V_{bi} - V)}{A^2 e \varepsilon_0 \varepsilon_r N_D} \quad (4)$$

where C is the value of the capacitance, V is the voltage applied in OSCs, A and e stand for electrode area (0.1 cm^2) and element charge, respectively, ε_r and ε_0 represent relative dielectric constant and vacuum permittivity, respectively, and N_D is the carrier density. Here, ε_r is determined by the capacitance value at a frequency (1 kHz) and V = 0 V in dark conditions according to the formula:[55]

$$C = \varepsilon_0 \varepsilon_r \frac{A}{d} \quad (5)$$

where d is the thickness of the photoactive layer (100 nm). The calculated values of ε_r, V_{bi}, and N_D are summarized in Table 4. According to Table 4, the values of V_{bi} were 0.59 V (w/o CILs), 0.72 V (PFN), and 0.81 V (PBTA-FN). V_{bi} gradually increased from PFN to PBTA-FN, resulting in a rightward shift in the Mott Schottky curves, as shown in Fig. 5b. In the OSCs with low V_{bi}, when the forward bias was higher than V_{bi}, the electric field in the devices reversed, hindering the carrier extraction.[56,57] The highest value of V_{bi} was obtained for the photovoltaic cell using PBTA-FN, which leads to a higher V_{oc} and FF, which was consistent with the result of dark current measurements. Moreover, the values of N_D calculated based on eqn (4) and (5) were 0.85 × 10^{16} cm^{-3} (w/o CILs), 1.34 × 10^{16} cm^{-3} (PFN) and 1.56 × 10^{16} cm^{-3} (PBTA-FN). The increased N_D and ε_r for photovoltaic devices using PBTA-FN should be responsible for the low series resistance.[58]

When the coulombic interactions between the electrons and the holes is equal to the thermal energy kT, the Coulomb capture radius (R_c) is defined as the distance between electrons and holes, which are related by the equation:[59]

$$R_c = \frac{e^2}{4\pi\varepsilon_0\varepsilon_r kT} \quad (6)$$

Table 4 Calculated dielectric parameters of OSCs under different conditions

CILs	V_{bi} (V)	$C_{1\ kHz}$ (nF)	ε_r	N_D (10^{16} cm^{-3})	R_c (nm)
w/o CILs	0.59	2.82	3.19	0.85	17.47
PFN	0.72	3.01	3.40	1.34	16.39
PBTA-FN	0.81	3.04	3.44	1.56	16.20

ε_r is obtained from eqn (5) and Table 4, when the frequency is at 1 kHz. Clearly, R_c is inversely proportional to ε_r, and the calculated results are listed in Table 4. These calculated values of R_c are 17.47 nm (w/o CILs), 16.39 nm (PFN) and 16.20 nm (PBTA-FN). The low R_c values indicated that the electrons and holes were hard to be captured by coulombic interactions in the diffusion process, which could suppress the bimolecular recombination and thus, a higher FF could be achieved.[60] Part of the reason for this phenomenon may be that the introduction of PBTA-FN enables the formation of a larger V_{bi} compared with PFN, and R_c was the result of the coulombic interactions and the built-in electric potential competing with each other.

According to Onsager theory, the exciton dissociation probability in an organic semiconductor is obtained from the equation:

$$P(E) = e^{-R_c/a}\left(1 + \frac{eR_c}{2kT}E\right) \quad (7)$$

where $P(E)$ stands for a probability that an exciton (electron–hole pair) separated as free charges, while $1 - P(E)$ represents the probability of geminate recombination, and E is electric field strength.[59] According to Onsager's theory, a ''hot'' electron transports some distance from its geminate holes through thermal energy. The ''a'' in the eqn (7) is defined as the thermalization distance between the electron and the hole.[59] The smallest R_c (16.20 nm) in the OSC device with PBTA-FN indicated that the introduction of PBTA-FN could result in a higher exciton dissociation rate and decrease the probability of geminate recombination.

Conclusion

In conclusion, a novel polymer named PBTA-FN with self-doping effect was designed and synthesized. The PCE of 12.18% for the PBDB-T-2F:IT-4F-based device was achieved with PBTA-FN as the CIL. The *J*–*V* curves under different light intensity and calculations of the Coulomb capture radius showed that the OSCs with PBTA-FN could effectively inhibit bimolecular recombination, resulting in the highest FF. The built-in electric potential was improved from 0.72 V (PFN processed) to 0.81 V (PBTA-FN processed), thus increasing the V_{oc}. The AFM and WCA test results on the surface of the active-layer/CIL suggested that the morphology hardly changed and the surface polarity improved; this should be attributed to the larger interface dipole of PBTA-FN. Thus, PBTA-FN can reduce the work function of the Al electrode and enhance the built-in electric potential, which was further confirmed by UPS and Mott Schottky curves. Above all, these results indicate that the main reasons for using self-doping PBTA-FN as a CIL to enhance PCE were large interface dipole (corresponding to high built-in potential), good ohmic contact and high electron mobility, which boosted the interface contact and charge extraction. These investigations indicate that the self-doped water/alcohol conjugated polymer with high mobility is a promising electron transport material for high-performance solution-processed OSCs.

Conflicts of interest

There are no conflicts to declare.

Acknowledgements

The authors thank the National Natural Science Foundation of China (no. 51602139), Excellent Team of Scientific Research (201705), the Foundation of A Hundred Youth Talents Training.

Notes and references

1 T. Liu, L. Huo, S. Chandrabose, K. Chen, G. Han, F. Qi, X. Meng, D. Xie, W. Ma, Y. Yi, J. M. Hodgkiss, F. Liu, J. Wang, C. Yang and Y. Sun, *Adv. Mater.*, 2018, 30, 1707353.
2 M. Li, K. Gao, X. Wan, Q. Zhang, B. Kan, R. Xia, F. Liu, X. Yang, H. Feng, W. Ni, Y. Wang, J. Peng, H. Zhang, Z. Liang, H. L. Yip, X. Peng, Y. Cao and Y. Chen, *Nat. Photonics*, 2017, 11, 85.
3 Z. Du, X. Bao, Y. Li, D. Liu, J. Wang, C. Yang, R. Wimmer, L. W. Stade, R. Yang and D. Yu, *Adv. Energy Mater.*, 2017, 8, 1701471.
4 K. Gao, L. Li, T. Lai, L. Xiao, Y. Huang, F. Huang, J. Peng, Y. Cao, F. Liu, T. P. Russell, R. A. J. Janssen and X. Peng, *J. Am. Chem. Soc.*, 2015, 137, 7282.
5 W. Chen, W. Shen, H. Wang, F. Liu, L. Duan, X. Xu, D. Zhu, M. Qiu, E. Wang and R. Yang, *Dyes Pigm.*, 2019, 166, 42.
6 T. Liu and A. Troisi, *Adv. Mater.*, 2013, 25, 1038.
7 K. Gao, J. Miao, L. Xiao, W. Deng, Y. Kan, T. Liang, C. Wang, F. Huang, J. Peng, Y. Cao, F. Liu, T. P. Russell, H. Wu and X. Peng, *Adv. Mater.*, 2016, 28, 4727.
8 W. Chen, G. Huang, X. Li, H. Wang, Y. Li, H. Jiang, N. Zheng and R. Yang, *ACS Appl. Mater. Interfaces*, 2018, 10, 42747.
9 T. H. Lee, M. A. Uddin, C. Zhong, S. Ko, B. Walker, T. Kim, Y. J. Yoon, S. Y. Park, A. J. Heeger, H. Y. Woo and J. Y. Kim, *Adv. Energy Mater.*, 2016, 6, 1600637.
10 K. Gao, S. B. Jo, X. Shi, L. Nian, M. Zhang, Y. Kan, F. Lin, B. Kan, B. Xu, Q. Rong, L. Shui, F. Liu, X. Peng, G. Zhou, Y. Cao and A. K. Y. Jen, *Adv. Mater.*, 2019, 31, 1807842.
11 L. Han, N. Uranbileg, S. Jiang, Y. Xie, H. Jiang, Z. Lan, D. Yu, X. Bao and R. Yang, *J. Mater. Chem. A*, 2019, 7, 10505.
12 S. Song, K. T. Lee, C. W. Koh, H. Shin, M. Gao, H. Y. Woo, D. Vak and J. Y. Kim, *Energy Environ. Sci.*, 2018, 11, 3248.
13 X. Bao, Y. Zhang, J. Wang, D. Zhu, C. Yang, Y. Li, C. Yang, J. Xu and R. Yang, *Chem. Mater.*, 2017, 29, 6766.
14 Z. Liang, J. Tong, H. Li, Y. Wang, N. Wang, J. Li, C. Yang and Y. Xia, *J. Mater. Chem. A*, 2019, 7, 15841.
15 W. Chen, H. Jiang, G. Huang, J. Zhang, M. Cai, X. Wan and R. Yang, *Sol. RRL*, 2018, 2,1800101.
16 T. Liu, Z. Luo, Q. Fan, G. Zhang, L. Zhang, W. Gao, X. Guo, W. Ma, M. Zhang, C. Yang, Y. Li and H. Yan, *Energy Environ. Sci.*, 2018, 11, 3275.
17 X. Wang, Z. Du, K. Dou, H. Jiang, C. Gao, L. Han and R. Yang, *Adv. Energy Mater.*, 2019, 9, 1802530.
18 K. Gao, Z. Zhu, B. Xu, S. B. Jo, Y. Kan, X. Peng and K. Y. Jen, *Adv. Mater.*, 2017, 29, 1703980.

19 C. Waldauf, M. Morana, P. Denk, P. Schilinsky, K. Coakley, S. A. Choulisa and C. J. Brabec, *Appl. Phys. Lett.*, 2006, 89, 233517.
20 M. S. White, D. C. Olson, S. E. Shaheen, N. Kopidakis and D. S. Ginley, *Appl. Phys. Lett.*, 2006, 89, 143517.
21 Y. Zhou, H. Cheun, W. P. Jr, C. Fuentes-Hernandez, S. J. Kim and B. Kippelen, *J. Mater. Chem.*, 2010, 20, 6189.
22 F. Huang, H. Wu, D. Wang, W. Yang and Y. Cao, *Chem. Mater.*, 2004, 16, 708.
23 X. Zhao, D. Madan, Y. Cheng, J. Zhou, H. Li, S. M. Thon, A. E. Bragg, M. E. Decoster, P. E. Hopkins and H. E. Katz, *Adv. Mater.*, 2017, 29, 1606928.
24 X. Lin, B. Wegner, K. M. Lee, M. A. Fusella, F. Zhang, K. Moudgil, B. P. Rand, S. Barlow, S. R. Marder, N. Koch and A. Kahn, *Nat. Mater.*, 2017, 16, 1209.
25 W. Chen, W. Jiao, D. Li, X. Sun, X. Guo, M. Lei, Q. Wang and Y. Li, *Chem. Mater.*, 2016, 28, 1227.
26 J. Liu, N. Zheng, Z. Hu, Z. Wang, X. Yang, F. Huang and Y. Cao, *Sci. China: Chem.*, 2017, 60, 1136.
27 J. Li, Z. Liang, Y. Wang, H. Li, J. Tong, X. Bao and Y. Xia, *J. Mater. Chem. C*, 2018, 6, 11015.
28 J. Tong, J. Li, P. Zhang, X. Ma, M. Wang, L. An, J. Sun, P. Guo, C. Yang and Y. Xia, *Polymer*, 2017, 121, 183.
29 J. Li, Y. Wang, Z. Liang, N. Wang, J. Tong, C. Yang, X. Bao and Y. Xia, *ACS Appl. Mater. Interfaces*, 2019, 11, 7022.
30 Z. Wu, C. Sun, S. Dong, X. Jiang, S. Wu, H. Wu, H. L. Yip, F. Huang and Y. Cao, *J. Am. Chem. Soc.*, 2016, 138, 2004.
31 Z. Hu, Z. Chen, K. Zhang, N. Zheng, R. Xie, X. Liu, X. Yang, F. Huang and Y. Cao, *Sol. RRL*, 2017, 1, 1700055.
32 Z. Hu, R. Xu, S. Dong, K. Lin, J. Liu, F. Huang and Y. Cao, *Mater. Horiz.*, 2017, 4, 88.
33 S. Grimme, S. Ehrlich and L. Goerigk, *J. Comput. Chem.*, 2011, 32, 1456.
34 L. Lu, T. Xu, W. Chen, E. S. Landry and L. Yu, *Nat. Photonics*, 2014, 8, 716.
35 V. Shrotriya, Y. Yao, G. Li and Y. Yang, *Appl. Phys. Lett.*, 2006, 89, 063505.
36 L. Nian, W. Zhang, N. Zhu, L. Liu, Z. Xie, H. Wu, F. Wurthner and Y. Ma, *J. Am. Chem. Soc.*, 2015, 137, 6995.
37 J. Wang, C. Yan, X. Zhang, X. Zhao, Y. Fu, B. Zhang and Z. Xie, *J. Mater. Chem. C*, 2016, 4, 10820.
38 E. Yao, C. Chen, J. Gao, Y. Liu, Q. Chen, M. Cai, W. C. Hsu, Z. Hong, G. Li and Y. Yang, *Sol. Energy Mater. Sol. Cells*, 2014, 130, 20.
39 Y. Zhang, S. Yuan, Y. Li and W. Zhang, *Electrochim. Acta*, 2014, 117, 438.
40 C. Dunkel, M. Wark, T. Oekermann, R. Ostermann and B. M. Smarsly, *Electrochim. Acta*, 2013, 90, 375.
41 Y. Wang, B. Wu, Z. Wu, Z. Lan, Y. Li, M. Zhang and F. Zhu, *J. Phys. Chem. Lett.*, 2017, 8, 5264.
42 S. Wang, Z. Li, X. Xu, G. Zhang, Y. Qi and Q. Peng, *Adv. Mater. Interfaces*, 2019, 6, 1801480.
43 G. A. H. Wetzelaer, M. Kuik, M. Lenes and P. W. M. Blom, *Appl. Phys. Lett.*, 2011, 99, 153506.
44 A. K. K. Kyaw, D. H. Wang, V. Gupta, W. L. Leong, L. Ke, G. C. Bazan and A. J. Heeger, *ACS Nano*, 2013, 7, 4569.
45 J. Wan, X. Xu, G. Zhang, Y. Li, K. Feng and Q. Peng, *Energy Environ. Sci.*, 2017, 10, 1739.
46 X. Gong, M. Tong, F. G. Brunetti, J. Seo, Y. Sun, D. Moses, F. Wudl and A. J. Heeger, *Adv. Mater.*, 2011, 23, 2272.
47 J. Luo, H. Wu, C. He, A. Li, W. Yang and Y. Cao, *Appl. Phys. Lett.*, 2009, 95, 043301.
48 S. R. Cowan, A. Roy and A. J. Heeger, *Phys. Rev. B: Condens. Matter Mater. Phys.*, 2010, 82, 245207.
49 L. Nian, W. Zhang, S. Wu, L. Qin, L. Liu, Z. Xie, H. Wu and Y. Ma, *ACS Appl. Mater. Interfaces*, 2015, 7, 25821.
50 X. Cheng, S. Sun, Y. Chen, Y. Gao, L. Ai, T. Jia, F. Li and Y. Wang, *J. Mater. Chem. A*, 2014, 2, 12484.
51 Q. Zhang, D. Zhang, X. Li, X. Liu, W. Zhang, L. Han and J. Fang, *Chem. Commun.*, 2015, 51, 10182.
52 T. H. Lai, S. W. Tsang, J. R. Manders, S. Chen and F. So, *Mater. Today*, 2013, 16, 424.
53 Z. Zhang, B. Qi, Z. Jin, D. Chi, Z. Qi, Y. Li and J. Wang, *Energy Environ. Sci.*, 2014, 7, 1966.
54 T. Schiros, G. Kladnik, D. Prezzi, A. Ferretti, G. Olivieri, A. Cossaro, L. Floreano, A. Verdini, C. Schenck, M. Cox, A. A. Gorodetsky, K. Plunkett, D. Delongchamp, C. Nuckolls, A. Morgante, D. Cvetko and I. Kymissis, *Adv. Energy Mater.*, 2013, 3, 894.
55 C. Zhan, X. Zhang and J. Yao, *RSC Adv.*, 2015, 5, 93002.
56 T. Kirchartz, W. Gong, S. A. Hawks, T. Agostinelli, R. C. I. MacKenzie, Y. Yang and J. Nelson, *J. Phys. Chem. C*, 2012, 116, 7672.
57 U. Rau, D. A. Ras and T. Kirchartz, *Advanced Characterization Techniques for Thin Film Solar Cells*, John Wiley & Sons, 2011.
58 C. Liu, D. Zhang, Z. Li, X. Zhang, W. Guo, L. Zhang, L. Shen, S. Ruan and Y. Long, *ACS Appl. Mater. Interfaces*, 2017, 9, 8830.
59 K. M. Pelzer and S. B. Darling, *Mol. Syst. Des. Eng.*, 2016, 1, 10.
60 M. B. Upama, N. K. Elumalai, M. A. Mahmud, M. Wright, D. Wang, C. Xu and A. Uddin, *Sol. Energy Mater. Sol. Cells*, 2018, 176, 109.